

Fermi-Liquid T^2 Resistivity: Dynamical Mean-Field Theory Meets Experiment

Jeremy Lee-Hand,^{1,*} Harrison LaBollita,^{2,*} Fabian B. Kugler,^{2,*} Lorenzo Van Muñoz,³ Jason Kaye,^{2,4} Sophie Beck,² Alexander Hampel,² Antoine Georges,^{5,2,6,7} and Cyrus E. Dreyer^{1,2,†}

¹*Department of Physics and Astronomy, Stony Brook University, Stony Brook, New York, 11794-3800, USA*

²*Center for Computational Quantum Physics, Flatiron Institute,
162 5th Avenue, New York, New York 10010, USA.*

³*Department of Physics, Massachusetts Institute of Technology,
77 Massachusetts Avenue, Cambridge, MA 02139, USA.*

⁴*Center for Computational Mathematics, Flatiron Institute,
162 5th Avenue, New York, New York 10010, USA.*

⁵*Collège de France, 11 place Marcelin Berthelot, 75005 Paris, France*

⁶*CPHT, CNRS, École Polytechnique, IP Paris, F-91128 Palaiseau, France*

⁷*DQMP, Université de Genève, 24 quai Ernest Ansermet, CH-1211 Genève, Suisse*

(Dated: December 24, 2024)

Direct-current resistivity is a key probe for the physical properties of materials. In metals, Fermi-liquid (FL) theory serves as the basis for understanding transport. A T^2 behavior of the resistivity is often taken as a signature of FL electron-electron scattering. However, the presence of impurity and phonon scattering as well as material-specific aspects such as Fermi surface geometry can complicate this interpretation. We demonstrate how density-functional theory combined with dynamical mean-field theory can be used to elucidate the FL regime. We take as examples SrVO_3 and SrMoO_3 , two moderately correlated perovskite oxides, and establish a precise framework to analyze the FL behavior of the self-energy at low energy and temperature. Reviewing published low-temperature resistivity measurements, we find agreement between our calculations and experiments performed on samples with exceptionally low residual resistivity. This comparison emphasizes the need for further theoretical, synthesis, and characterization developments in these and other FL materials.

The direct-current (DC) resistivity as a function of temperature, $\rho(T)$, is a fundamental probe in solid-state physics. In metals, $\rho(T)$ typically increases as a power law of T , the specific form of which in principle differentiates between distinct scattering mechanisms. A cornerstone of such an analysis is Fermi-liquid (FL) theory [1], which provides a robust framework for understanding interacting fermions. A key prediction of the theory is the $\rho \propto T^2$ scaling originating from electron-electron (el-el) Umklapp scattering [2] (for a recent discussion, see [3]).

For materials with strong correlations, the el-el contribution to ρ often dominates. However, in systems with more moderate correlations, revealing FL behavior is challenging because of other sources of scattering. Depending on the relative strength of el-el and electron-phonon (el-ph) scattering, the true el-el-dominated FL regime may occur only at very low T . Furthermore, it has recently become clear that some of the traditional assumptions about the low- T scaling of el-ph scattering (such as the often assumed T^5 law [4, 5]) may be complicated by material-dependent properties such as the shape of the Fermi surface [6–8]. The intrinsic low- T behavior of ρ may also be obscured by the residual resistivity from impurities and disorder, hence requiring high-quality samples. Therefore, a robust comparison between experiments and *ab-initio* theory, where different contributions to ρ can be cleanly separated, is of great value

for understanding the transport properties of metals.

Here, we focus on two materials where FL behavior is often invoked, the perovskite oxides SrVO_3 and SrMoO_3 . For SrVO_3 , extensive transport studies [7, 9–24] demonstrated $\rho \propto T^2$ up to room temperature (RT), though the interpretation of this as arising from FL el-el scattering has been debated [7, 23, 25]. A similar behavior is observed for SrMoO_3 , which has the lowest RT resistivity of any perovskite oxide [26]. However, there have been relatively few transport measurements on this material.

In this work, we show that dynamical mean-field theory combined with density functional theory (DFT+DMFT) [27, 28] successfully elucidates the low- T FL behavior in both of these materials. A thorough examination of published data reveals agreement between our calculations and experiments and also provides motivations for new transport measurements. Computing transport properties at low T in metals is challenging, since the el-el scattering rate must be evaluated to a high degree of precision. We achieve this goal thanks to recent algorithmic advances and careful analysis of the numerical data. Fundamental questions on the theory of transport raised by our findings are also emphasized.

We begin by reviewing the experimental situation for the DC resistivities of SrVO_3 and SrMoO_3 . In Fig. 1, we plot ρ versus T^2 extracted from several selected [33] experimental works differentiated by single-crystal samples versus epitaxial films. For both materials, the curves appear to follow a $\rho(T) = \rho_0 + AT^2$ trend up to RT. Interestingly, for SrVO_3 , the reported single-crystal data [22–24] have higher A coefficients and higher residual re-

* These authors contributed equally to this work.

† Corresponding author, cyrus.dreyer@stonybrook.edu

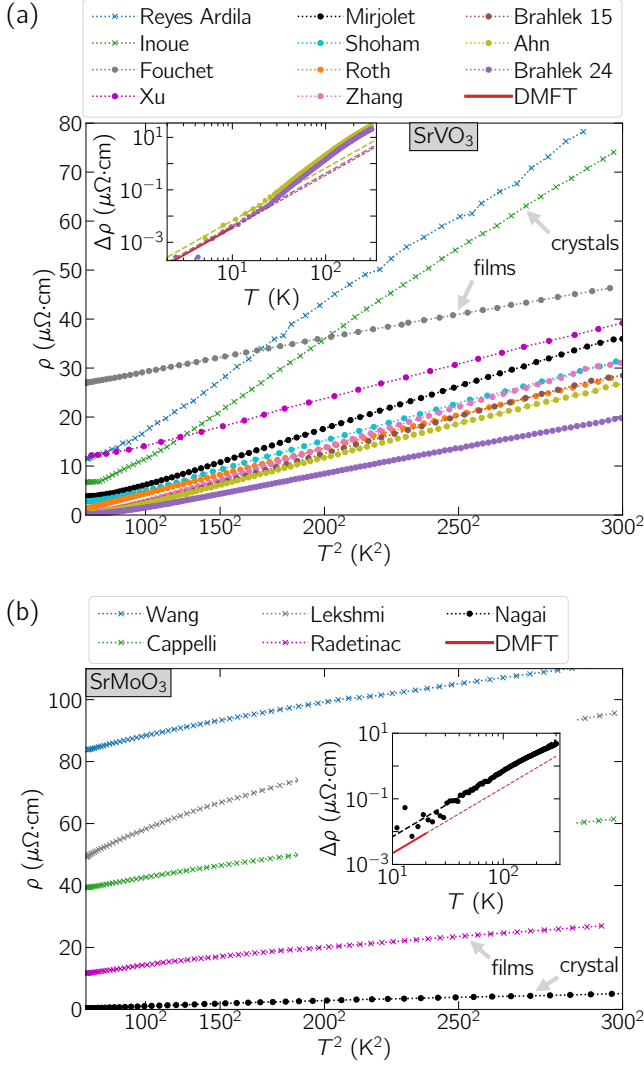


FIG. 1. Resistivity measurements versus T^2 on a linear scale for (a) SrVO_3 and (b) SrMoO_3 , extracted from Refs. 7, 12–19, 22, 23, 26, 29–32. The inset in (a) shows $\Delta\rho = \rho - \rho_0$, with ρ_0 the $T = 0$ residual resistivity, for the data from Ahn *et al.* [12] and Brahlek *et al.* [17], clearly showing two different T^2 regimes above and below ~ 20 K. The inset in (b) shows the same for the data from Nagai *et al.* [26].

sistivities ρ_0 than most thin films [7, 12–21], while for SrMoO_3 the lone single-crystal result [26] has by far the lowest A and ρ_0 compared to films [29–32].

In the low- ρ_0 films of SrVO_3 [12, 17], there are actually *two* regimes of approximately T^2 behavior, separated by a crossover around 20–30 K [17]. This is clearly seen in the inset of Fig. 1(a), showing $\Delta\rho = \rho - \rho_0$ from Refs. 12 and 17 on a log-log scale. This effect was attributed [25] to a crossover between el-el- and el-ph-dominated scattering and is difficult to resolve in samples with higher ρ_0 . The inset of Fig. 1(b) indicates that a similar behavior may be present in the data from Ref. 26 for SrMoO_3 , although the low- T resolution is more limited.

A quantitative analysis of the experimental $\rho(T)$ is given in Table I in the End Matter. We fit the curves of Fig. 1 to extract A in two regimes: (i) T up to RT and (ii) T up to 20 K (50 K) for SrVO_3 (SrMoO_3). We also extract ρ_0 by extrapolating the curves to $T = 0$ [34] and order them by their residual-resistivity ratios (RRRs).

For SrVO_3 , consistent with Fig. 1(a), one finds a clear differentiation between the single-crystal and film results; we focus on the films since they exhibit the lowest ρ_0 's and largest RRRs. The A coefficients fit up to RT are in the range $2\text{--}4 \times 10^{-4} \mu\Omega \cdot \text{cm}/\text{K}^2$, while the spread of A 's fit below 20 K illustrates the challenges of resolving small ρ in the presence of impurity scattering. For films with a larger RRR (and also lower ρ_0), A is about an order of magnitude smaller than the values fit up to RT. As shown below, if we interpret this low- T regime to be the one dominated by el-el scattering [17, 25], its A coefficient agrees with our DFT+DMFT result within error bars. For SrMoO_3 , the inset of Fig. 1(b) indicates that the low- T T^2 regime of ρ in the high-quality (single-crystal) sample [26] is not fully resolved. Interestingly, the data points below 30 K seem to fall below the RT T^2 behavior, potentially indicating a lower value of the A coefficient at low T . As shown below, this interpretation is consistent with our DFT+DMFT calculations.

We now turn to our computational framework. The low-energy models for SrVO_3 and SrMoO_3 are derived from DFT by downfolding the Kohn–Sham bands onto Wannier-like t_{2g} orbitals. The low-energy models are solved within single-site DMFT using both continuous-time quantum Monte Carlo (QMC) in the hybridization expansion (CT-HYB) as implemented in the TRIQS software [35–38] and the numerical renormalization group (NRG) [39] in an implementation [40–43] based on the QSpace tensor library [44–46]. For the QMC imaginary-frequency solver, Padé analytic continuation (AC) is used to obtain low-energy real-frequency data. For the NRG real-frequency solver, using the recently developed symmetric improved estimator for the self-energy is crucial for fine low-energy resolution [47]. Further computational details are given in the End Matter and in Ref. [48].

We compute the conductivity within DMFT using the Kubo formula neglecting vertex corrections (consistent with the momentum independence of the DMFT self-energy and vertex [49, 50]). For SrVO_3 and SrMoO_3 in their cubic crystal settings, the t_{2g} orbitals are degenerate and the self-energy is band independent, $\Sigma_{\nu\nu'}(\omega, T) = \delta_{\nu\nu'}\Sigma(\omega, T)$, which enables the following simplifications. We consider $2|\text{Im}\Sigma(0, T)| \ll T \ll \epsilon_F$, where ϵ_F is the Fermi energy and $k_B = \hbar = e = 1$. As interband contributions are negligible in the DC limit, one then finds [51, 52]

$$\rho(T) = \left[\Phi(\epsilon_F) \int_{-\infty}^{+\infty} d\omega \left(-\frac{df}{d\omega} \right) \frac{1}{2|\text{Im}\Sigma(\omega, T)|} \right]^{-1}. \quad (1)$$

Here, f is the Fermi–Dirac distribution function and

$\Phi_{\alpha\alpha'}(\epsilon_F) = \delta_{\alpha\alpha'}\Phi(\epsilon_F)$ the transport function at ϵ_F ,

$$\Phi_{\alpha\alpha'}(\epsilon_F) = 2 \sum_{\nu} \int_{\text{BZ}} \frac{d^d k}{(2\pi)^d} v_{\nu}^{\alpha}(\mathbf{k}) v_{\nu}^{\alpha'}(\mathbf{k}) \delta(\epsilon_F - \epsilon_{\nu\mathbf{k}}), \quad (2)$$

where d is the dimensionality, $v_{\nu}^{\alpha}(\mathbf{k})$ the velocity of band ν and k -point \mathbf{k} in direction α , and $\epsilon_{\nu\mathbf{k}}$ its energy. For a FL, the self-energy fulfills to leading order in ω and T

$$\text{Im}\Sigma(\omega, T) \simeq -C(\omega^2 + \pi^2 T^2). \quad (3)$$

Plugging Eq. (3) into Eq. (1) eventually gives the FL DC resistivity to leading order as

$$\rho(T) \simeq AT^2, \quad A = 24C/\Phi(\epsilon_F). \quad (4)$$

The transport function is obtained by iterative adaptive integration [53] leveraging Wannier interpolation using the Julia library AUTOBZ.JL [54, 55]. C can be extracted from the DMFT self-energy, $\text{Im}\Sigma$, for $T < T^{\text{FL}}$, where T^{FL} denotes the scale below which FL behavior holds (i.e., Eq. (3) applies in the absence of other sources of inelastic scattering than el-el). The small scattering rates of SrVO_3 and SrMoO_3 make the accurate extraction of C a challenging task [48]. To ensure this is achieved, we demonstrate consistency between DMFT solvers (QMC and NRG) and between extracting C from Σ on the imaginary- or real-frequency axis. We begin with the latter case, where we plot in Fig. 2 $-\text{Im}\Sigma(\omega, T)/(\pi T)^2$ versus $|\omega|/T$ on a log-log scale for $T = 116, 193$, and 290 K. According to the FL form (3), the curves from different T should collapse onto the universal form $C[\omega^2/(\pi T)^2 + 1]$. Indeed, we see from Fig. 2, that there is an approximate collapse. This establishes that these temperatures are below T^{FL} for both materials, as independently confirmed by our $T = 0$ NRG results for the spin susceptibility (see [48]). Note that the presence of el-ph interactions in experiments requires measurements at very low T , while we can explore FL behavior in a broader T range in our calculations involving only el-el interactions.

We found that the QMC+Padé results for $|\omega| < T$ depend sensitively on the AC parameters, particularly the value of η when evaluating the Padé approximant at $\omega + i\eta$ (see [48]). NRG results for $|\omega| < T$ are also less reliable than for $|\omega| > T$ since the Wilson chain is effectively cut on the scale of T [45, 56, 57]. Importantly, however, the QMC+Padé results for $\omega \gtrsim T$ are stable with respect to the AC parameters [48] and in very good agreement with NRG. This allows us to robustly determine the value of C (the error bar/shaded region is chosen to span the spread of the curves in Fig. 2) as $0.45 \pm 0.15 \text{ eV}^{-1}$ for SrVO_3 [58] and $0.48 \pm 0.13 \text{ eV}^{-1}$ for SrMoO_3 .

The insets in Fig. 2 show the real part of the self-energy, related to the quasiparticle weight Z as

$$1 - 1/Z = \partial_{\omega} \text{Re}\Sigma(\omega, T)|_{\omega=0}. \quad (5)$$

From both QMC and NRG, we find $Z \approx 0.50$ for SrVO_3 and $Z \approx 0.59$ for SrMoO_3 (for all T considered in Fig. 2).

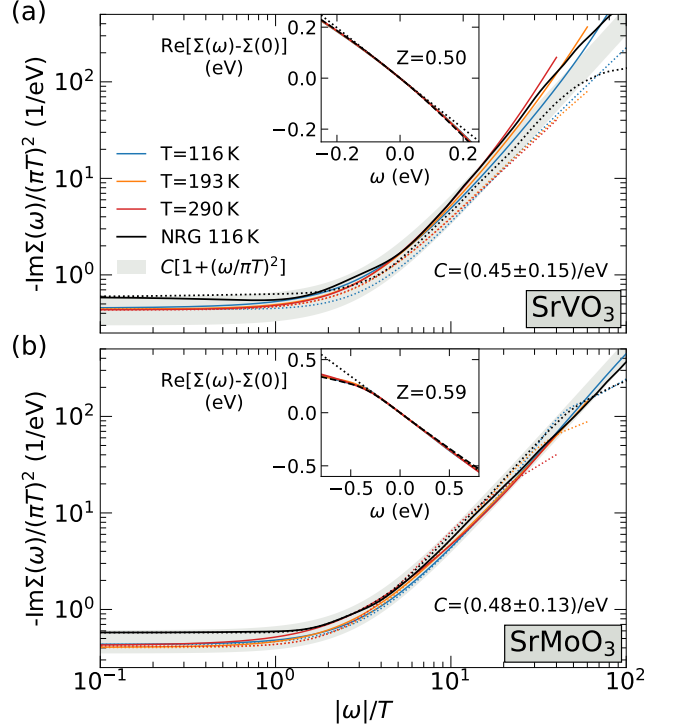


FIG. 2. $-\text{Im}\Sigma(\omega)/(\pi T)^2$ as a function of $|\omega|/T$ for SrVO_3 and SrMoO_3 on a log-log scale. Solid (dotted) lines denote $\omega > 0$ ($\omega < 0$). Colored (black) lines are obtained with QMC (NRG). Shaded regions indicate a confidence region for the FL collapse to $C[\omega^2/(\pi T)^2 + 1]$. Inset shows $\text{Re}\Sigma(\omega, T) - \text{Re}\Sigma(0, T)$ compared with $1 - 1/Z = \partial_{\omega} \text{Re}\Sigma(\omega, T)|_{\omega=0}$.

We can confirm these results by analyzing Σ in imaginary frequencies, thus removing the need for AC of the QMC data. To this end, we translate the FL forms (3) and (5) to Matsubara frequencies $i\omega_n = i(2n+1)\pi T$, $n \in \mathbb{Z}$,

$$\text{Im}\Sigma(i\omega_n, T) \simeq (1 - 1/Z)\omega_n + \text{sgn}(\omega_n)C(\omega_n^2 - \pi^2 T^2). \quad (6)$$

The two parameters Z and C can be inferred from polynomial fits to a few data points of $\text{Im}\Sigma(i\omega_n, T)$. As discussed in [48], we find that extracting $\text{Im}\Sigma(i0^+, T)$ from the zeroth-order coefficient of the fit is very sensitive to the choice of numerical parameters, while obtaining C via the quadratic coefficient is more stable. This is analogous to the real-frequency case discussed above, where the AC for $|\omega| < T$ was found to be problematic.

Here, we find it most convenient to solve for Z and C when evaluating Eq. (6) at the first two Matsubara points. We therefore define [59]

$$1 - \frac{1}{Z_T} = \frac{\text{Im}\Sigma(i\pi T)}{\pi T}, \quad C_T = \frac{\text{Im}\Sigma(3i\pi T) - 3\text{Im}\Sigma(i\pi T)}{8\pi^2 T^2}. \quad (7)$$

It is easy to see that, at low T , $Z_T = Z + \mathcal{O}(T^2/T_{\text{FL}}^2)$ [60] and $C_T = C + \mathcal{O}(T/T_{\text{FL}})$. The main panels of Fig. 3 show $\text{Im}\Sigma(i\omega_n, T)$, demonstrating the agreement between QMC and NRG. The insets show how Z_T and

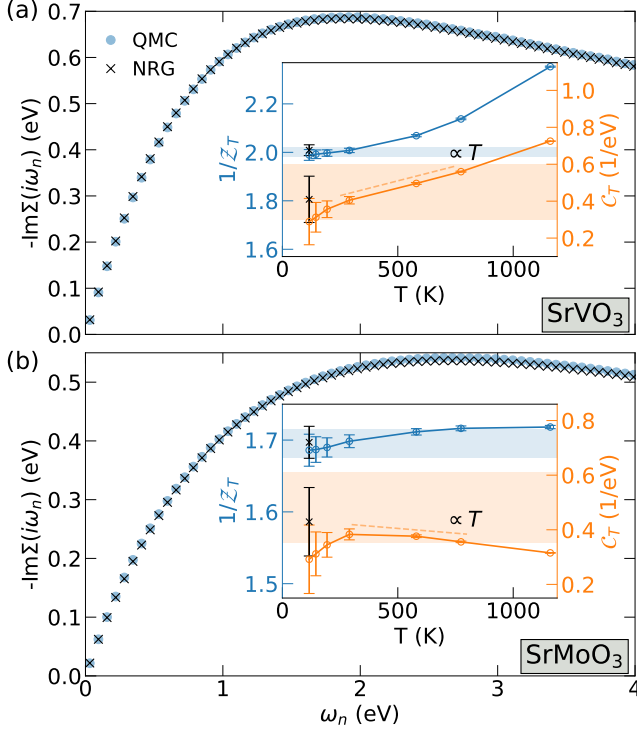


FIG. 3. $-\text{Im}\Sigma(i\omega_n)$ at $T = 116$ K for SrVO_3 and SrMoO_3 , from QMC and NRG. Insets show $1/Z_T$ and C_T computed from Eq. (7) for decreasing T . Error bars show how, by way of example, an error of 0.7 meV on $\text{Im}\Sigma(i\omega_n)$ propagates to $1/Z_T$ and C_T . Shaded regions indicate the range of values estimated from our real-frequency analysis in Fig. 2.

C_T converge with decreasing T to the values determined from our real-frequency analysis—although the expression for C_T becomes unstable to noise in $\text{Im}\Sigma$ at low T .

Using Eq. (4) to convert C to A coefficients (in units of $10^{-5} \mu\Omega\cdot\text{cm}/\text{K}^2$) gives 3.6 ± 1.2 for SrVO_3 and 2.2 ± 0.6 for SrMoO_3 (see Table I). We plot these results in the insets of Fig. 1. For SrVO_3 , there is remarkable agreement with the low- T T^2 regime of the highest-quality thin films, indicating the importance of el-el scattering in this regime [17, 25]. For the SrMoO_3 single-crystal data, the true low- T behavior is not fully resolved, but appears to be consistent with a transition to a T^2 regime given by our A coefficient. The fact that the A coefficients of both materials are similar indicates that the significant difference in RT resistivity between the two oxides is not due to different degrees of electron correlation.

FL materials are often categorized by their so-called Kadowaki–Woods ratio [61–65] (KWR) A/γ^2 . We compute the specific-heat coefficient γ via the density of states at the Fermi level $D(\epsilon_F)$ and Z ,

$$\gamma = \frac{\pi^2 D(\epsilon_F)}{3Z}, \quad D(\epsilon_F) = 2 \sum_{\nu} \int_{\text{BZ}} \frac{d^d k}{(2\pi)^d} \delta(\epsilon_F - \epsilon_{\nu \mathbf{k}}). \quad (8)$$

The results for the molar quantity γ_0 [64] in units of $\text{mJ}/(\text{mol}\cdot\text{K}^2)$ are 7.9 for SrVO_3 and 7.5 for SrMoO_3 , in

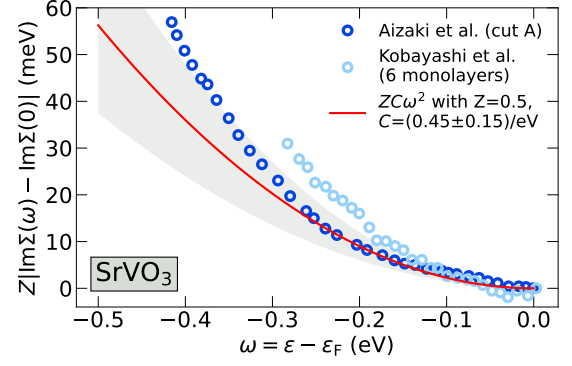


FIG. 4. Comparison between DMFT self-energy and ARPES momentum distribution curves (MDCs) for SrVO_3 , the latter taken from Aizaki *et al.* [71] and Kobayashi *et al.* [72] (both measured below 20 K). We use $2Z|\text{Im}\Sigma(\omega)| \approx \hbar v_F^* \Delta k$, where Δk is the MDC FWHM and we extracted the renormalized Fermi velocity as $\hbar v_F^* = 0.54 \text{ eV}\cdot\text{\AA}$ from ARPES [71].

good agreement with the reported experimental values: 8.2 for SrVO_3 [23] and 7.9 for SrMoO_3 [26]. Hence, the KWR in units of $\mu\Omega\cdot\text{cm}\cdot\text{mol}^2\text{K}^2/\text{J}^2$ is 0.6 for SrVO_3 and 0.4 for SrMoO_3 . The KWR we find for SrVO_3 is more than an order of magnitude below the value of 10 reported for single crystals [23]. Our results thus cause the KWR of SrVO_3 to fall off the trend of other correlated oxides [64] (e.g., $\text{Sr}_3\text{Ru}_2\text{O}_7$ [66]), but puts it, along with SrMoO_3 , in good agreement with elemental transition metals (e.g., Re or Fe) [61]. This is suggestive of the fact that SrVO_3 and SrMoO_3 are rather moderately correlated and consistent with the argument of Ref. 63 that weakly correlated systems (where T^{FL} is comparable to ϵ_F) would have a KWR similar to the transition metals.

In strongly correlated materials like UPt_3 [67] and cuprates [68–70], the A coefficient is basically independent of impurity concentration. However, for the moderately correlated SrVO_3 and SrMoO_3 , there appears to be a correlation between the reported values of A and ρ_0 (or anticorrelation between A and RRR). Whether this is an experimental issue or indicates a breakdown of the simple picture in which impurities and disorder contribute a T -independent scattering rate via Matthiessen’s rule is an important topic for further investigation. To settle this question, it is crucial to determine the origin of the discrepancy between single crystals and thin films in these materials, motivating further investigation on high-quality single crystals in the low- T regime.

Finally, we comment on fundamental implications of our work for transport theory. Our calculations use the *single-site* DMFT approximation, where vertex corrections to the conductivity are absent due to the locality of the self-energy and vertex [49]. However, vertex corrections were shown to be important in specific regimes, such as low-dimensional systems [73–76] and the low-density limit [77, 78]. In the low-density limit, phase-space considerations limit the possibility of Umklapp

lapp scattering, and it was shown in Ref. 78 that $|\text{Im}\Sigma|$ is severely underestimated by DMFT in this regime (note, though, that the case of a cylindrical Fermi surface, relevant to the present oxides, still needs to be explored along similar lines). In contrast to systems with very small Fermi surfaces like doped SrTiO_3 [79, 80], Umklapp scattering *is* possible for SrVO_3 . In Fig. 4, we compare our DMFT self-energy with angle-resolved photoemission spectroscopy (ARPES). The excellent agreement at low frequencies suggests that the possible underestimation of $|\text{Im}\Sigma|$ does not apply here and provides a confirmation, independent of transport measurements, that single-site DMFT yields reliable results for the FL behavior of SrVO_3 . Nevertheless, the effect of vertex corrections to ρ remains to be explored.

In summary, we showed that single-site DFT+DMFT can accurately describe the FL properties of SrVO_3 and SrMoO_3 , two materials with moderate electron correlations. For SrVO_3 , we obtain an A coefficient in agreement with the low- T value for the best thin-film samples. Clarifying the experimental situation regarding the discrepancy with single-crystal measurements in this context is desirable. For SrMoO_3 , our A coefficient is lower than the fit to the experimental data. However, the ex-

perimental low- T behavior is not fully resolved, and future experiments may reveal a lower- T el-el-dominated T^2 regime as in SrVO_3 . This work thus serves as an impetus for more extensive transport measurements and computations for moderately correlated materials, as well as to elucidate fundamental aspects of transport theory, like the relevance of vertex corrections. Experimentally, the crossover between the el-ph and el-el dominated regimes should be explored in spectroscopy alongside with transport. Overall, our work demonstrates the importance of synergetic developments in *ab-initio* theory and materials synthesis/characterization to advance the understanding of transport in quantum materials.

ACKNOWLEDGMENTS

We are grateful to Kamran Behnia, Gaël Grissonnanche, Nigel Hussey, Andy Millis, Jernej Mravlje, Cyril Proust, and Louis Taillefer, and Philip Allen for useful discussions. The authors thank Naoki Shirakawa for sending us the data of Ref. 26. C.E.D. and J.L.H. acknowledge support from the National Science Foundation under Grant No. DMR-2237674. The Flatiron Institute is a division of the Simons Foundation.

-
- [1] L. D. Landau, The Theory of a Fermi Liquid, *Zh. Eksp. Teor. Fiz.* **30**, 1058 (1956).
 - [2] L. D. Landau and I. Y. Pomeranchuk, On the properties of metals at very low temperatures, *Sov. J. Exp. Theor. Phys.* **7**, 379 (1937).
 - [3] K. Behnia, On the Origin and the Amplitude of T-Square Resistivity in Fermi Liquids, *Ann. Phys.* **534**, 2100588 (2022).
 - [4] J. Ziman, *Electrons and phonons: the theory of transport phenomena in solids* (Oxford university press, 1960).
 - [5] P. B. Allen, New method for solving Boltzmann's equation for electrons in metals, *Phys. Rev. B* **17**, 3725 (1978).
 - [6] C. A. Kukkonen, T^2 electrical resistivity due to electron-phonon scattering on a small cylindrical Fermi surface: Application to bismuth, *Phys. Rev. B* **18**, 1849 (1978).
 - [7] M. Mirjole, F. Rivadulla, P. Marsik, V. Borisov, R. Valentí, and J. Fontcuberta, Electron-phonon coupling and electron-phonon scattering in SrVO_3 , *Adv. Sci.* **8**, 2004207 (2021).
 - [8] D. J. Abramovitch, J.-J. Zhou, J. Mravlje, A. Georges, and M. Bernardi, Combining electron-phonon and dynamical mean-field theory calculations of correlated materials: Transport in the correlated metal Sr_2RuO_4 , *Phys. Rev. Mater.* **7**, 093801 (2023).
 - [9] A. Nozaki, H. Yoshikawa, T. Wada, H. Yamauchi, and S. Tanaka, Layered perovskite compounds $\text{Sr}_{n+1}\text{V}_n\text{O}_{3n+1}$ ($n = 1, 2, 3$, and ∞), *Phys. Rev. B* **43**, 181 (1991).
 - [10] M. Itoh, M. Shikano, H. Kawaji, and T. Nakamura, Structural aspects on the variations of electric and magnetic properties of the layered compound system $\text{Sr}_{n+1}\text{V}_n\text{O}_{3n+1-\delta}$ ($n = 1, 2, 3, \infty$), *Solid State Commun.* **80**, 545 (1991).
 - [11] Y. Lan, X. Chen, and M. He, Structure, magnetic susceptibility and resistivity properties of SrVO_3 , *J. Alloys Compd.* **354**, 95 (2003).
 - [12] G. Ahn, M. Zingl, S. J. Noh, M. Brahlek, J. D. Roth, R. Engel-Herbert, A. J. Millis, and S. J. Moon, Low-energy interband transition in the infrared response of the correlated metal SrVO_3 in the ultraclean limit, *Phys. Rev. B* **106**, 085133 (2022).
 - [13] R. Xu, Y. Ji, R. Bouchilaoun, F. Qian, M. Li, X. Zhang, R. Tang, R. Zhao, S. Misra, H. Wang, W. Li, C. Kan, D. Shi, J. Fan, and H. Yang, Optical and electrical properties of (111)-oriented epitaxial SrVO_3 thin films, *Ceram. Int.* **45**, 11304 (2019).
 - [14] J. Roth, T. Kuznetsova, L. Miao, A. Pogrebnyakov, N. Alem, and R. Engel-Herbert, Self-regulated growth of [111]-oriented perovskite oxide films using hybrid molecular beam epitaxy, *APL Mater.* **9**, 021114 (2021).
 - [15] A. Fouchet, M. Allain, B. Bérini, E. Popova, P.-E. Janolin, N. Guiblin, E. Chikoidze, J. Scola, D. Hrabovsky, Y. Dumont, and N. Keller, Study of the electronic phase transition with low dimensionality in SrVO_3 thin films, *Mater. Sci. Eng. B* **212**, 7 (2016).
 - [16] M. Brahlek, L. Zhang, C. Eaton, H.-T. Zhang, and R. Engel-Herbert, Accessing a growth window for SrVO_3 thin films, *App. Phys. Lett.* **107**, 143108 (2015).
 - [17] M. Brahlek, J. D. Roth, L. Zhang, M. Briggeman, P. Irvin, J. Lapano, J. Levy, T. Birol, and R. Engel-Herbert, Hidden transport phenomena in an ultraclean correlated metal, *Nat. Commun.* **15**, 5304 (2024).
 - [18] L. Shoham, M. Baskin, M.-G. Han, Y. Zhu, and L. Kornblum, Scalable synthesis of the transparent conductive

- oxide SrVO₃, *Adv. Electron. Mater.* **6**, 1900584 (2020).
- [19] L. Zhang, Y. Zhou, L. Guo, W. Zhao, A. Barnes, H.-T. Zhang, C. Eaton, Y. Zheng, M. Brahlek, H. F. Haneef, N. J. Podraza, M. H. Chan, V. Gopalan, K. M. Rabe, and R. Engel-Herbert, Correlated metals as transparent conductors, *Nat. Materials* **15**, 204 (2016).
- [20] M. Mirjolet, F. Sánchez, and J. Fontcuberta, High carrier mobility, electrical conductivity, and optical transmittance in epitaxial SrVO₃ thin films, *Adv. Funct. Mater.* **29**, 1808432 (2019).
- [21] M. Mirjolet, H. B. Vasili, A. Valadkhani, J. Santiso, V. Borisov, P. Gargiani, M. Valvidares, R. Valentí, and J. Fontcuberta, Orbital occupancy and hybridization in strained SrVO₃ epitaxial films, *Phys. Rev. Mater.* **5**, 095002 (2021).
- [22] D. Reyes Ardila, J. Andreeta, and H. Basso, Preparation, microstructural and electrical characterization of SrVO₃ single crystal fiber, *J. Crys. Growth* **211**, 313 (2000).
- [23] I. H. Inoue, O. Goto, H. Makino, N. E. Hussey, and M. Ishikawa, Bandwidth control in a perovskite-type 3d¹-correlated metal Ca_{1-x}Sr_xVO₃. I. Evolution of the electronic properties and effective mass, *Phys. Rev. B* **58**, 4372 (1998).
- [24] T. Berry, S. Bernier, G. Auffermann, T. M. McQueen, and W. Adam Phelan, Laser floating zone growth of SrVO₃ single crystals, *J. Crys. Growth* **583**, 126518 (2022).
- [25] D. J. Abramovitch, J. Mravlje, J.-J. Zhou, A. Georges, and M. Bernardi, Respective roles of electron-phonon and electron-electron interactions in the transport and quasiparticle properties of SrVO₃, *Phys. Rev. Lett.* **133**, 186501 (2024).
- [26] I. Nagai, N. Shirakawa, S. I. Ikeda, R. Iwasaki, H. Nishimura, and M. Kosaka, Highest conductivity oxide SrMoO₃ grown by a floating-zone method under ultralow oxygen partial pressure, *App. Phys. Lett.* **87**, 2 (2005).
- [27] A. Georges, G. Kotliar, W. Krauth, and M. J. Rozenberg, Dynamical mean-field theory of strongly correlated fermion systems and the limit of infinite dimensions, *Rev. Mod. Phys.* **68**, 13 (1996).
- [28] G. Kotliar, S. Y. Savrasov, K. Haule, V. S. Oudovenko, O. Parcollet, and C. A. Marianetti, Electronic structure calculations with dynamical mean-field theory, *Rev. Mod. Phys.* **78**, 865 (2006).
- [29] H. Wang, D. Cui, Y. Zhou, Z. Chen, F. Chen, T. Zhao, H. Lu, G. Yang, M. Xu, Y. Lan, X. Chen, H. Qian, and F. Liu, Growth and characterization of SrMoO₃ thin films, *J. Crys. Growth* **226**, 261 (2001).
- [30] E. Cappelli, A. Hampel, A. Chikina, E. B. Guedes, G. Gatti, A. Hunter, J. Issing, N. Biskup, M. Varela, C. E. Dreyer, A. Tamai, A. Georges, F. Y. Bruno, M. Radovic, and F. Baumberger, Electronic structure of the highly conductive perovskite oxide SrMoO₃, *Phys. Rev. Mater.* **6**, 075002 (2022).
- [31] I. C. Lekshmi, A. Gayen, and M. Hegde, The effect of strain on nonlinear temperature dependence of resistivity in SrMoO₃ and SrMoO_{3-x}N_x films, *Mater. Res. Bull.* **40**, 93 (2005).
- [32] A. Radetinac, J. Zimmermann, K. Hoyer, H. Zhang, P. Komissinskiy, and L. Alff, Optical properties of single crystalline SrMoO₃ thin films, *J. App. Phys.* **119**, 055302 (2016).
- [33] Where data for multiple samples are presented, we take the highest RRR sample. For SrVO₃, we exclude previous powder results [9–11] and the recent single-crystal results of Ref. 24 due to the very large ρ_0 (though Ref. 24 is included in Table I). We also exclude Ref. 81 due to difficulties in extracting the data from the plots and Ref. 82 due to lacking low-*T* measurements. The data for Mirjolet *et al.* are from Ref. 7.
- [34] This was done by fitting the digitized data to $\rho(T) = \rho_0 + AT^2$ either below 20 K, or 50 K if the fits to 20 K could not be achieved.
- [35] O. Parcollet, M. Ferrero, T. Ayral, H. Hafermann, I. Krivenko, L. Messio, and P. Seth, TRIQS: A toolbox for research on interacting quantum systems, *Comp. Phys. Commun.* **196**, 398 (2015).
- [36] M. Aichhorn, L. Pourovskii, P. Seth, V. Vildosola, M. Zingl, O. Peil, X. Deng, J. Mravlje, G. Kraberger, C. Martins, M. Ferrero, and O. Parcollet, TRIQS/DFTTools: A TRIQS application for ab initio calculations of correlated materials, *Comp. Phys. Commun.* **204**, 200 (2016).
- [37] P. Seth, I. Krivenko, M. Ferrero, and O. Parcollet, TRIQS/CTHYB: A continuous-time quantum Monte Carlo hybridisation expansion solver for quantum impurity problems, *Comp. Phys. Commun.* **200**, 274 (2016).
- [38] M. E. Merkel, A. Carta, S. Beck, and A. Hampel, solid.dmf: gray-boxing DFT+DMFT materials simulations with TRIQS, *J. Open Source Softw.* **7**, 4623 (2022).
- [39] R. Bulla, T. A. Costi, and T. Pruschke, Numerical renormalization group method for quantum impurity systems, *Rev. Mod. Phys.* **80**, 395 (2008).
- [40] F. B. Kugler, S.-S. B. Lee, A. Weichselbaum, G. Kotliar, and J. von Delft, Orbital differentiation in Hund metals, *Phys. Rev. B* **100**, 115159 (2019).
- [41] F. B. Kugler, M. Zingl, H. U. R. Strand, S.-S. B. Lee, J. von Delft, and A. Georges, Strongly correlated materials from a numerical renormalization group perspective: How the Fermi-liquid state of Sr₂RuO₄ emerges, *Phys. Rev. Lett.* **124**, 016401 (2020).
- [42] F. B. Kugler and G. Kotliar, Is the orbital-selective Mott phase stable against interorbital hopping?, *Phys. Rev. Lett.* **129**, 096403 (2022).
- [43] F. B. Kugler, C.-J. Kang, and G. Kotliar, Low-energy perspective on two-orbital Hund metals and the case of LaNiO₂, *Phys. Rev. B* **110**, 155101 (2024).
- [44] A. Weichselbaum, Non-abelian symmetries in tensor networks: A quantum symmetry space approach, *Ann. Phys.* **327**, 2972 (2012).
- [45] A. Weichselbaum, Tensor networks and the numerical renormalization group, *Phys. Rev. B* **86**, 245124 (2012).
- [46] A. Weichselbaum, X-symbols for non-abelian symmetries in tensor networks, *Phys. Rev. Res.* **2**, 023385 (2020).
- [47] F. B. Kugler, Improved estimator for numerical renormalization group calculations of the self-energy, *Phys. Rev. B* **105**, 245132 (2022).
- [48] J. Lee-Hand, H. LaBollita, F. B. Kugler, L. van Muñoz, S. Beck, A. Hampel, J. Kaye, A. Georges, and C. E. Dreyer, Contribution of electron-electron scattering on electrical transport in cubic perovskite metals from dynamical mean-field theory, Unpublished (2024).
- [49] A. Khurana, Electrical conductivity in the infinite-dimensional Hubbard model, *Phys. Rev. Lett.* **64**, 1990 (1990).
- [50] G. Uhrig and D. Vollhardt, Drude weight and DC conductivity of correlated electrons, *Phys. Rev. B* **52**, 5617 (1995).

- [51] C. Berthod, J. Mravlje, X. Deng, R. Žitko, D. van der Marel, and A. Georges, Non-Drude universal scaling laws for the optical response of local Fermi liquids, *Phys. Rev. B* **87**, 115109 (2013).
- [52] A. Georges and J. Mravlje, Skewed non-Fermi liquids and the Seebeck effect, *Phys. Rev. Res.* **3**, 043132 (2021).
- [53] Results are converged to four digits at 1 meV broadening for both the transport function and the density of states.
- [54] J. Kaye, S. Beck, A. Barnett, L. V. Muñoz, and O. Parcollet, Automatic, high-order, and adaptive algorithms for Brillouin zone integration, *SciPost Phys.* **15**, 062 (2023).
- [55] L. V. Muñoz, S. Beck, and J. Kaye, `AutoBZ.jl`: automatic, adaptive Brillouin-zone integration of Wannier-interpolated response functions, in preparation.
- [56] A. Weichselbaum and J. von Delft, Sum-rule conserving spectral functions from the numerical renormalization group, *Phys. Rev. Lett.* **99**, 076402 (2007).
- [57] S.-S. B. Lee and A. Weichselbaum, Adaptive broadening to improve spectral resolution in the numerical renormalization group, *Phys. Rev. B* **94**, 235127 (2016).
- [58] Note that this number is slightly larger than 0.33 eV^{-1} reported in Ref. 25; we show in [48] that this discrepancy comes solely from the method of extracting A from Σ .
- [59] To simplify notations, the explicit dependence of Σ on T is omitted in this equation. Note that, when performing a linear fit to the first two Matsubara data points, the slope yields $1 - 1/Z + 4C\pi T$, but the offset corresponds to $-4C\pi^2 T^2$, hence a factor of 4 times $\text{Im}\Sigma(\omega = 0, T)$. The factor 8 in the denominator of the estimator of C used in the main text properly accounts for this.
- [60] A. V. Chubukov and D. L. Maslov, First-Matsubara-frequency rule in a Fermi liquid. I. Fermionic self-energy, *Phys. Rev. B* **86**, 155136 (2012).
- [61] M. J. Rice, Electron-electron scattering in transition metals, *Phys. Rev. Lett.* **20**, 1439 (1968).
- [62] K. Kadowaki and S. Woods, Universal relationship of the resistivity and specific heat in heavy-fermion compounds, *Solid State Commun.* **58**, 507 (1986).
- [63] K. Miyake, T. Matsuura, and C. Varma, Relation between resistivity and effective mass in heavy-fermion and A15 compounds, *Solid State Commun.* **71**, 1149–1153 (1989).
- [64] N. E. Hussey, Non-generality of the Kadowaki–Woods ratio in correlated oxides, *J. Phys. Soc. Japan* **74**, 1107–1110 (2005).
- [65] A. Jacko, J. Fjærestad, and B. Powell, A unified explanation of the Kadowaki–Woods ratio in strongly correlated metals, *Nat. Phys.* **5**, 422 (2009).
- [66] K. Behnia, On the dynamic distinguishability of nodal quasi-particles in overdoped cuprates, *SciPost Phys.* **12**, 200 (2022).
- [67] R. Joynt and L. Taillefer, The superconducting phases of UPt_3 , *Rev. Mod. Phys.* **74**, 235 (2002).
- [68] F. Rullier-Albenque, H. Alloul, and R. Tourbot, Disorder and transport in cuprates: Weak localization and magnetic contributions, *Phys. Rev. Lett.* **87**, 157001 (2001).
- [69] F. Rullier-Albenque, H. Alloul, and R. Tourbot, Influence of pair breaking and phase fluctuations on disordered high T_c cuprate superconductors, *Phys. Rev. Lett.* **91**, 047001 (2003).
- [70] D. Juskus, J. Ayres, R. Nicholls, and N. E. Hussey, Insensitivity of T_c to the residual resistivity in high- T_c cuprates and the tale of two domes, *Front. Phys.* **12** (2024).
- [71] S. Aizaki, T. Yoshida, K. Yoshimatsu, M. Takizawa, M. Minohara, S. Ideta, A. Fujimori, K. Gupta, P. Mahadevan, K. Horiba, H. Kumigashira, and M. Oshima, Self-energy on the low- to high-energy electronic structure of correlated metal SrVO_3 , *Phys. Rev. Lett.* **109**, 056401 (2012).
- [72] M. Kobayashi, K. Yoshimatsu, T. Mitsuhashi, M. Kitamura, E. Sakai, R. Yukawa, M. Minohara, A. Fujimori, K. Horiba, and H. Kumigashira, Emergence of quantum critical behavior in metallic quantum-well states of strongly correlated oxides, *Sci. Rep.* **7**, 16621 (2017).
- [73] P. T. Brown, D. Mitra, E. Guardado-Sanchez, R. Nourafkan, A. Reymbaut, C.-D. Hébert, S. Bergeron, A.-M. S. Tremblay, J. Kokalj, D. A. Huse, P. Schauf, and W. S. Bakr, Bad metallic transport in a cold atom Fermi-Hubbard system, *Science* **363**, 379 (2019).
- [74] J. Vučičević, J. Kokalj, R. Žitko, N. Wentzell, D. Tanasković, and J. Mravlje, Conductivity in the square lattice Hubbard model at high temperatures: Importance of vertex corrections, *Phys. Rev. Lett.* **123**, 036601 (2019).
- [75] A. Vranić, J. Vučičević, J. Kokalj, J. Skolimowski, R. Žitko, J. Mravlje, and D. Tanasković, Charge transport in the Hubbard model at high temperatures: Triangular versus square lattice, *Phys. Rev. B* **102**, 115142 (2020).
- [76] J. Vučičević, S. Predin, and M. Ferrero, Charge fluctuations, hydrodynamics, and transport in the square-lattice Hubbard model, *Phys. Rev. B* **107**, 155140 (2023).
- [77] A. Mu, Z. Sun, and A. J. Millis, Optical conductivity of the two-dimensional Hubbard model: Vertex corrections, emergent Galilean invariance, and the accuracy of the single-site dynamical mean field approximation, *Phys. Rev. B* **106**, 085142 (2022).
- [78] A. Mu, Z. Sun, and A. J. Millis, Adequacy of the dynamical mean field theory for low density and Dirac materials, *Phys. Rev. B* **109**, 115154 (2024).
- [79] X. Lin, B. Fauqué, and K. Behnia, Scalable T^2 resistivity in a small single-component Fermi surface, *Science* **349**, 945 (2015).
- [80] D. van der Marel, J. L. M. van Mechelen, and I. I. Mazin, Common Fermi-liquid origin of T^2 resistivity and superconductivity in n -type SrTiO_3 , *Phys. Rev. B* **84**, 205111 (2011).
- [81] V. Giannakopoulou, P. Odier, J. Bassat, and J. Loup, SrVO_3 and Sr_2VO_4 , electrical properties below and above room T, *Solid State Commun.* **93**, 579 (1995).
- [82] T. Maekawa, K. Kurosaki, H. Muta, M. Uno, and S. Yamanaka, Thermal and electrical properties of perovskite-type strontium molybdate, *J. Alloys Compd.* **390**, 314 (2005).
- [83] G. Kresse and J. Hafner, Ab initio molecular dynamics for liquid metals, *Phys. Rev. B* **47**, 558 (1993).
- [84] G. Kresse and J. Furthmüller, Efficient iterative schemes for ab initio total-energy calculations using a plane-wave basis set, *Phys. Rev. B* **54**, 11169 (1996).
- [85] G. Kresse and D. Joubert, From ultrasoft pseudopotentials to the projector augmented-wave method, *Phys. Rev. B* **59**, 1758 (1999).
- [86] A. A. Mostofi, J. R. Yates, Y.-S. Lee, I. Souza, D. Vanderbilt, and N. Marzari, wannier90: A tool for obtaining maximally-localised Wannier functions, *Comp. Phys. Commun.* **178**, 685 (2008).

- [87] F. Lechermann, A. Georges, A. Poteryaev, S. Biermann, M. Posternak, A. Yamasaki, and O. K. Andersen, Dynamical mean-field theory using Wannier functions: A flexible route to electronic structure calculations of strongly correlated materials, *Phys. Rev. B* **74**, 125120 (2006).
- [88] A. Hampel, S. Beck, and C. Ederer, Effect of charge self-consistency in DFT + DMFT calculations for complex transition metal oxides, *Phys. Rev. Res.* **2**, 033088 (2020).
- [89] A. Sekiyama, H. Fujiwara, S. Imada, S. Suga, H. Eisaki, S. I. Uchida, K. Takegahara, H. Harima, Y. Saitoh, I. A. Nekrasov, G. Keller, D. E. Kondakov, A. V. Kozhevnikov, T. Pruschke, K. Held, D. Vollhardt, and V. I. Anisimov, Mutual experimental and theoretical validation of bulk photoemission spectra of $\text{Sr}_{1-x}\text{Ca}_x\text{VO}_3$, *Phys. Rev. Lett.* **93**, 156402 (2004).
- [90] E. Pavarini, S. Biermann, A. Poteryaev, A. I. Lichtenstein, A. Georges, and O. K. Andersen, Mott transition and suppression of orbital fluctuations in orthorhombic $3d^1$ perovskites, *Phys. Rev. Lett.* **92**, 176403 (2004).
- [91] I. A. Nekrasov, K. Held, G. Keller, D. E. Kondakov, T. Pruschke, M. Kollar, O. K. Andersen, V. I. Anisimov, and D. Vollhardt, Momentum-resolved spectral functions of SrVO_3 calculated by LDA + DMFT, *Phys. Rev. B* **73**, 155112 (2006).
- [92] K. Maiti, U. Manju, S. Ray, P. Mahadevan, I. H. Inoue, C. Carbone, and D. D. Sarma, Understanding the bulk electronic structure of $\text{Ca}_{1-x}\text{Sr}_x\text{VO}_3$, *Phys. Rev. B* **73**, 052508 (2006).
- [93] J. Kaufmann, C. Eckhardt, M. Pickem, M. Kitatani, A. Kauch, and K. Held, Self-consistent ladder dynamical vertex approximation, *Phys. Rev. B* **103**, 035120 (2021).

TABLE I. Fermi-liquid T^2 coefficient A (fitted up to 300 K and at low- T , i.e., up to 20 K for SrVO₃ and 50 K for SrMoO₃), extrapolated zero-temperature resistivity ρ_0 , and residual-resistivity ratio RRR from experimental measurements compared to the DMFT result for A of this work. Dashes indicate that the fitting was not possible from the digitized data. Values in square brackets are those explicitly reported in the reference.

		A ($10^{-5}\mu\Omega\cdot\text{cm}/\text{K}^2$)				
		Fit to 300 K	low- T fit	ρ_0 ($\mu\Omega\cdot\text{cm}$)	RRR	
SrVO_3	Single crystal	Berry <i>et al.</i> [24]	526.8 [520.0]	–	176.6 [172.4]	3.5 [3.6]
		Reyes Ardila <i>et al.</i> [22]	81.6 [83.0]	–	[11.3]	6.8 [6.0]
		Inoue <i>et al.</i> [23]	78.8	[42.1] ^a	[6.3]	11.0
	Thin film	Fouchet <i>et al.</i> [15]	22.3 [22.1]	34.2	27.0 [27.0]	1.7 [2.0]
		Xu <i>et al.</i> [13]	31.2 [27.7]	–	11.3 [6.8]	3.4
		Mirjolet <i>et al.</i> [7]	37.3 [30.0]	7.0	3.7	9.7 [9.6]
		Shoham <i>et al.</i> [18]	32.8 [33.5]	–	2.8 [2.9]	11.1 [11.2]
		Roth <i>et al.</i> [14]	30.5	11.8	1.4 [1.3]	20.4 [21.0]
		Zhang <i>et al.</i> [19]	35.6	7.9	0.3	95.9
		Brahlek <i>et al.</i> (2015) [16]	32.7	4.9	0.2 [0.2]	122.6 [125]
		Ahn <i>et al.</i> [12]	30.3	6.7	0.2	126.2 [130]
		Brahlek <i>et al.</i> (2024) [17]	22.4	4.2	0.1 [0.1]	185.7 [195.0]
	DMFT		3.6 ± 1.2			
SrMoO_3	Thin film	Wang <i>et al.</i> [29]	48.0	50.6	83.7	1.3
		Cappelli <i>et al.</i> [30]	37.0 [37.7 \pm 7]	27.3	39.3 [39.3]	1.6 [1.5]
		Lekshmi <i>et al.</i> [31]	74.3	93.3	49.1 [35.7]	2.0 [1.9]
		Radetinac <i>et al.</i> [32]	27.4	25.7	11.6	2.3
	Single crystal	Nagai <i>et al.</i> [26]	7.1 [7.0] ^b	7.0	0.35 [0.35]	14 [14]
	DMFT		2.2 ± 0.6			

^a Here, the authors used a fit up to 300 K, but including an el-ph T^5 contribution in the fit. Thus, A reflects the low- T behavior.

^b Here, the high- T fit is done up to 150 K instead of 300 K. Our low- T fit is done from 10 K to 50 K and yields the same ρ_0 and A .

END MATTER

Computational details. We compute the Kohn–Sham bands for cubic SrVO₃ ($a = 3.863$ Å) and SrMoO₃ ($a = 4.007$ Å) using the *Vienna ab-initio simulation package* (VASP) [83–85]. Using Wannier90 [86], we downfold the transition-metal t_{2g} -like bands onto a Wannier basis, which defines the impurity problem. We solve the quantum impurity problem in imaginary time using the QMC CT-HYB solver built on top of the TRIQS software stack [35–37] with `solid.dmft` as the driver of the DMFT loop [38], or in real frequencies using NRG (exploiting U(1) charge, SU(2) spin and SO(3) orbital symmetries [44]) as described in the main text. Both the QMC and NRG solvers use the same Wannier Hamiltonian as input. A Hubbard–Kanamori Hamiltonian including spin-flip and pair-hopping terms governs the interactions with $U = 4.5$ eV and $J = 0.65$ eV for SrVO₃ [87] and $U = 3.07$ eV and $J = 0.31$ eV for SrMoO₃ [88]. For additional computational details, see [48]. See [89–92] for early works on SrVO₃ or, e.g., [93] for a list of references.

Units and values of DFT properties. Restoring the prefactor $\hbar e^2$ for the transport function Φ , the latter has units $\hbar e^2 \text{cm}^{-3} (\text{eV cm}/\hbar)^2 \text{eV}^{-1}$. Recognizing e^2/\hbar as the conductance quantum, this immediately simplifies to $\text{eV}/(\Omega \text{cm})$. The precise values are

$$\text{SrVO}_3: \Phi(\epsilon_F) = \frac{2.247 \text{ eV}}{\text{m}\Omega \text{cm}}, \quad \text{SrMoO}_3: \Phi(\epsilon_F) = \frac{3.930 \text{ eV}}{\text{m}\Omega \text{cm}}. \quad (9)$$

It follows that A has units $(\Omega \text{cm})/\text{eV}^2$. Restoring a prefactor k_B^2 , one obtains A in units $(\Omega \text{cm})/K^2$ and $\rho \sim AT^2$ in units Ωcm . The density of states D as defined in the main text has units $\text{eV}^{-1} \text{cm}^{-3}$. However, for the molar specific-heat coefficient, the result is multiplied by the volume of the unit cell V_{uc} . The relevant values thus are

$$\text{SrVO}_3: V_{\text{uc}} D(\epsilon_F) = \frac{1.685}{\text{eV}}, \quad \text{SrMoO}_3: V_{\text{uc}} D(\epsilon_F) = \frac{1.886}{\text{eV}}. \quad (10)$$